Structural disorder in the decagonal Al–Co–Ni. II. Modeling

Miroslav Kobas,[1] Thomas Weber,[1] and Walter Steurer[1,2]
[1]*Laboratory of Crystallography, Department of Materials, ETH Zurich, Wolfgang-Pauli-Strasse 10, CH-8093 Zurich, Switzerland*
[2]*MNF, University of Zurich, Switzerland*
(Received 15 November 2004; revised manuscript received 15 February 2005; published 27 June 2005)

The hydrodynamic theory of phasonic and phononic disorder is applied successfully to describe the short-range disordered structure of a decagonal $Al_{71.5}Co_{14.6}Ni_{13.9}$ quasicrystal (*Edagawa phase*, superstructure type I). Moreover, model calculations demonstrate that the main features of diffuse scattering can be equally well described by phasonic disorder and fivefold orientational disorder of clusters. The calculations allow us to distinguish the different cluster types published so far and the best agreement with experimental data could be achieved with the mirror-symmetric Abe cluster. Modeling of phason diffuse scattering associated with the *S*1 and *S*2 superstructure reflections indicate disorder of superclusters. The former show basically intercluster correlations inside quasiperiodic layers, while the latter exhibit intra- and inter-cluster correlations, both between adjacent and inside quasiperiodic layers. The feasibility, potential, and limits of the Patterson method in combination with the *punch-and-fill* method employed is shown on the example of a phasonic disordered rhombic Penrose tiling. A variation of the elastic constants does not change qualitatively the way phasonic disorder is realized in the *local* quasicrystalline structure. For the same model system it is also shown that phasonic fluctuations of the atomic surfaces yield average clusters in the cut space, which correspond to fivefold orientationally disordered clusters.

DOI: 10.1103/PhysRevB.71.224206 PACS number(s): 61.44.Br, 61.43.Bn, 61.10.Nz

I. INTRODUCTION

The aim of this study is the modeling of structural disorder phenomena in decagonal Al–Co–Ni quasicrystals. Disorder in quasicrystals is primarily associated with phasonic disorder, which can be described with the hydrodynamic theory using the elastic properties of a fictitious *n*-dimensional (*n*D) hypercrystal. Although phasonic disorder has often been used to describe disorder in quasicrystals [see Refs. 1–6 and references therein], it is quite unclear, however, what it means in terms of 3D structural disorder.

One of the tasks of this study was to explore the applicability of the hydrodynamic theory of phasonic diffuse scattering (PDS) on *decagonal* quasicrystals and to check whether or not phasonic disorder is capable to describe the disordered structure of decagonal Al–Co–Ni. Emphasis was placed on the identification of local disorder phenomena inside the fundamental, columnar clusters of decagonal Al–Co–Ni quasicrystals as well as on the study of the 3D structural interpretation of phasonic disorder. The unsolved problem about the quasiperiodic superstructure of the *Edagawa phase* was tackled by a study of the structural disorder associated with the superstructure ordering.

The methods used in this study include the calculation of phasonic diffuse scattering (PDS) and thermal diffuse scattering (TDS) for a model system, a decorated rhombic Penrose tiling (RPT), as well as for synchrotron diffraction data taken on decagonal $Al_{71.5}Co_{14.6}Ni_{13.9}$, a superstructure of type I [*Edagawa phase*[7]]. In addition, modeling of disorder on the scale of clusters is used to identify local disorder phenomena and to distinguish between the different cluster types suggested in the literature.

In the following, we will briefly review theoretical work on PDS and TDS and then present current cluster models employed in our disorder model calculations.

II. PREVIOUS WORK

A. PDS and TDS

Within the framework of the hydrodynamic theory, Jaric and Nelson[8] developed a theory of diffuse scattering from icosahedral quasicrystals due to spatially fluctuating thermal and quenched strains. This approach was extended such that it could be used also for decorated quasilattices.[9–11] Lei *et al.* discussed both quenched and thermal phasons and phonons in the case of decagonal quasicrystals.[9] Ishii[12] pointed out that anisotropic diffuse scattering of phasonic origin in decagonal quasicrystals may only be expected in the case of strong phonon-phason coupling.

Yang *et al.*[13] and Hu *et al.*[14] investigated point groups and elastic properties of pentagonal and decagonal quasicrystals. The number of independent second-order elastic constants of Laue class $10/mmm$ has been determined: Five elastic constants are associated with the phonon field, three with the phason field, and one with the phonon-phason coupling. Phasonic elastic constants from geometrical random tilings have been calculated by Monte Carlo simulations.[15–17] Zhu and Henley[18] have estimated the phonon-phason coupling constant from relaxation simulations of an icosahedral quasicrystal model. A similar method has been applied to a simple decagonal quasicrystal model and the full set of elastic constants has been calculated.[19]

The hydrodynamic theory for quasicrystals predicts that the phonon displacement field relaxes rapidly via phonon modes, whereas the phason displacement field relaxes diffusively with much longer relaxation times.[20] At higher temperatures, the hydrodynamic theory treats phasons analogous to phonons, i.e., thermal excitations, and they are described

in a unified way. At lower temperatures, however, atomic diffusion is very sluggish and phonons will equilibrate in the presence of a quenched phason displacement field.[8,11,21] In this case phonons and phasons have to be treated separately.

B. Cluster models

A large number of cluster models for fundamental building units of decagonal Al–Co–Ni has been proposed [for a review see Steurer (Ref. 22)]. In the present work, the following most reasonable models were used for modeling structural diffuse scattering phenomena:

- Abe cluster:[23,24] d-$Al_{72}Co_8Ni_{20}$ (Ni-rich basic phase), periodicity ≈4 Å, columnar cluster with ≈20 Å diameter, mirror symmetry, forces a strictly quasiperiodic tiling.
- Hiraga-cluster:[25–27] d-$Al_{70}Co_{15}Ni_{15}$, periodicity ≈4 Å, diameter ≈20 Å, pentagonal symmetry [Refs. 25 and 26]. d-$Al_{72}Co_8Ni_{20}$, diameter ≈32 Å, pentagonal symmetry [Ref. 27]. Cluster model for the *Edagawa phase*: four-layer structure with sequence A, B, A', B', periodicity ≈8 Å, layers A and A' are flat, layers B and B' are puckered, layers A and A' act as mirror planes between layers B and B', diameter of ≈32 Å, pentagonal symmetry [Ref. 27].
- Ritsch-cluster:[28,29] d-$Al_{72.5}Co_{20}Ni_{7.5}$ (Co-rich basic phase), periodicity ≈4 Å, diameter ≈20 Å, pentagonal symmetry.
- Saitoh-cluster:[30] d-$Al_{72}Co_8Ni_{20}$ (Ni-rich basic phase), periodicity ≈4 Å, diameter ≈20 Å, mirror symmetry, consists of pentagonally shaped subclusters (P subcluster) and starlike shaped (S subcluster).
- Steinhardt cluster:[31,32] d-$Al_{72}Co_8Ni_{20}$ (Ni-rich basic phase), periodicity ≈4 Å, diameter ≈20 Å, mirror symmetry, *Gummelt* cluster covering[33] introduced that favors strict quasiperiodic tiling.
- Steurer cluster:[34] d-$Al_{70}Co_{15}Ni_{15}$, periodicity ≈4 Å, diameter ≈20 Å, 10_5 screw axis, layer A shows pentagonal symmetry, layer B mirror symmetry.
- Yan-cluster:[35–38] d-$Al_{72}Co_8Ni_{20}$ (Ni-rich basic phase), periodicity ≈4 Å, diameter ≈20 Å, substitutional disorder between transition metal (TM) atoms and Al in the core region of the cluster lowering the symmetry from pentagonal to mirror symmetry. Such a disordered model favors a random tiling structure [Ref. 35]. Slight modification based on P subclusters [Refs. 36–38].

All but the cluster model of Steurer *et al.*,[34] which has been derived by x-ray single-crystal structure analysis, are based on electron microscopy (EM) studies. The cluster of Hiraga *et al.*[25–27] and Ritsch *et al.*[28,29] exhibit 5m symmetry, all other models show mirror symmetry only.

III. EXPERIMENT

Alloys in the ternary system Al–Co–Ni with the nominal composition $Al_{72.5}Co_{14}Ni_{13.5}$ were prepared by Lemster[39] by producing compacts (pressure of 30 kN applied for 1 min, weight 5 g) of high-purity elements under argon atmosphere (Mbraun glove box 150 B-G, PanGas Ar 99.9998%). The stoichiometric formula $Al_{71.5}Co_{14.6}Ni_{13.9}$ was determined by electron microprobe x-ray analyzer with the wavelength dispersive method (CAMECA SX50, ±0.1 at. %). The compacts were melted twice in an arc furnace with water-cooled copper crucible (Degussa VOLiO, Hanan, Germany) for homogenization. Afterward they were put in an alumina crucible with top cover and were remelted in a high vacuum furnace (PVA MOV 64) under the following temperature conditions: heating up from 300 to 1470 K in 1 h, holding the temperature for 15 min, then cooling down with a rate of 0.5 K/min to 1120 K, holding the temperature for 4 h and subsequently cooling down to ambient temperature by switching off the high-vacuum furnace. The ingots of the different compacts were crushed and single crystals selected. The quality of the crystals was studied with x-ray photographic techniques.

The x-ray data collection of the Bragg reflection dataset (d-$Al_{71.5}Co_{14.6}Ni_{13.9}$) was performed at the four-circle diffractometer beamline $D3$ at the synchrotron source Hasylab ($\lambda = 0.56000$ Å, $3° \leqslant 2\Theta \leqslant 140°$, 15 474 reflections measured, therefrom 7058 main reflections, 4214 first order satellite reflections $S1$, and 4202 second-order satellite reflections $S2$).[40] Indexing of the satellite reflections here and in the following is after Edagawa *et al.*[7] The quasicrystal parameters $a = 3.7805(5)$ Å and $c = 4.0816(5)$ Å are defined such that the reciprocal parameters a^* and c^* correspond to the physical reciprocal-space lengths of the (10000) and (00001) reflections in the standard embedding, respectively [see Steurer, Ref. 34].

The experimental details on the image plate datasets of the *Edagawa phase* (d-$Al_{70}Co_{12}Ni_{18}$) are described in part I of our study.

IV. MODELING PDS AND TDS OF A RHOMBIC PENROSE TILING

A RPT has been constructed from its four-dimensional representation in the standard embedding as described in Cervellino *et al.*[41] The centers of the atomic surfaces (AS) of the RPT occupy the positions $\{(p/5, p/5, p/5, p/5)_D | p = 1, \ldots, 4\}$ on the body diagonal of the four-dimensional unit cell (subscript D denotes D basis). The ASs consist of four pentagons of radius $2a/5\tau^2$ at $p = 1, 4$ and of radius $2a/5\tau$ at $p = 2, 3$, where $\tau = (1+\sqrt{5})/2$ is the golden mean and $a = 3.757$ Å is the quasicrystal parameter. Throughout this paper, the "radius" of a regular polygon is defined as its center-to-vertex distance. Orientation of the ASs are according to Steurer and Haibach.[42] The ASs at $p = 1, 4$ are decorated with Ni atoms, the ones at $p = 2, 3$ with Al atoms. The chemical composition of the corresponding RPT [section of the tiling is depicted in Fig. 11(b)] is $Al_{61.8}Ni_{38.2}$. The atomic scattering factors are taken from Maslen *et al.*[43] Both the anisotropic atomic displacement parameters and the anisotropic phasonic parameters are set to zero for the calculation of the diffraction patterns of the RPT. The atomic configurations in parallel space are obtained through a cut of the four-dimensional embedding space by the two-dimensional parallel space.

A. Methodology: PDS and TDS calculations

For the calculation of PDS and TDS of a two-dimensional diffraction pattern, one has to solve the following expression

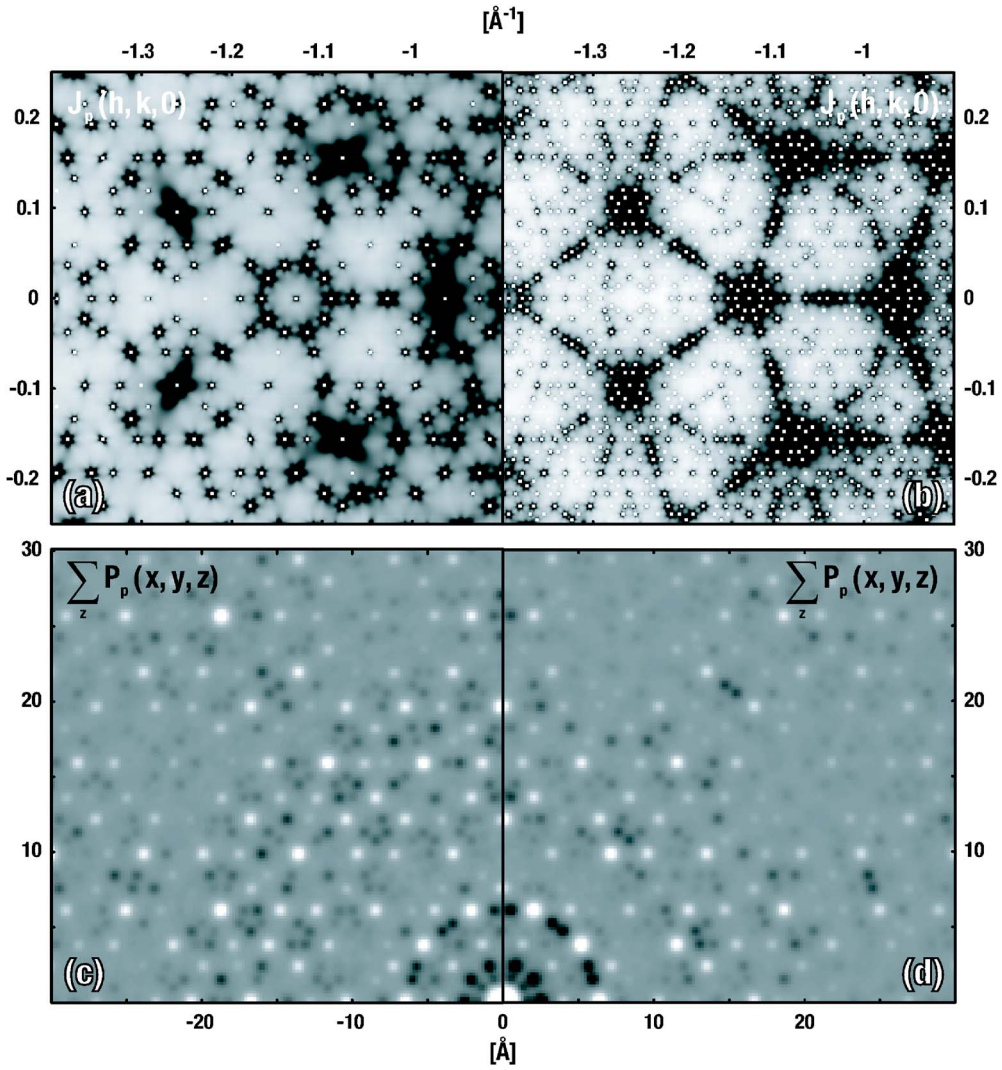

FIG. 1. Influence of a limitation of the perpendicular-space component of the diffraction vectors in reciprocal and Patterson space. Zoomed sections of calculated PDS and TDS of a RPT is shown for two datasets with a maximal perpendicular-space component of $d^*_{\perp,\max}=2$ Å^{-1} (a) and $d^*_{\perp,\max}=5$ Å^{-1} (b). The corresponding PMs are shown in (c) and (d), respectively. Diffuse "streaks" in (b) evolve because of the superposition of PDS from weak Bragg reflections with high perpendicular-space components. The PMs of both datasets are almost equivalent for short Patterson vectors and do only differ in fine structure details. Relative scaling of the intensities in the patterns (c) and (d) is 1:2.

for every single Bragg reflection (details on the theory can be found in Refs. 9–11)

$$\Delta J(\mathbf{R}^*_\parallel+\mathbf{o}^*_\parallel)=\frac{k_BT}{(2\pi)^3}\cdot J_{\text{aver}}(\mathbf{R}^*_\parallel)\cdot(\mathbf{R}^*_\parallel,\mathbf{R}^*_\perp)_V\cdot\mathbf{A}^{-1}(\mathbf{o}^*_\parallel)\cdot(\mathbf{R}^*_\parallel,\mathbf{R}^*_\perp)_V. \quad (1)$$

$\Delta J(\mathbf{R}^*_\parallel+\mathbf{o}^*_\parallel)$ is the diffuse intensity at offset $\mathbf{o}^*_\parallel$ from a particular Bragg reflection $\mathbf{R}^*_D=(\mathbf{R}^*_\parallel,\mathbf{R}^*_\perp)_V$ (subscript D denotes D basis, and V stands for the V basis), k_B is the Boltzmann constant, T is the temperature, $J_{\text{aver}}(\mathbf{R}^*_\parallel)$ is the Bragg scattering intensity of a particular reflection and $\mathbf{A}(\mathbf{o}^*_\parallel)$ is the hydrodynamic matrix. $\mathbf{A}(\mathbf{o}^*_\parallel)$ includes information on the elastic properties of the quasicrystal and, therefore, is also a function of the phononic elastic constants C_{ijkl}, of the phasonic elastic constants K_{ijkl}, and of the phonon-phason coupling constants R_{ijkl}. Note that Eq. (1) is valid in the case of simultaneously thermalized phonons and phasons ($T\geqslant T_q$, with T_q being the phason-quenching temperature). In the case of quenched phasons ($T<T_q$), Eq. (1) can still be written in the same form but $\mathbf{A}(\mathbf{o}^*_\parallel)$ has to be replaced by an effective hydrodynamic matrix $\mathbf{A}_{eff}(\mathbf{o}^*_\parallel)$. $\mathbf{A}_{eff}(\mathbf{o}^*_\parallel)$ is associated with C_{ijkl}, K_{ijkl}, R_{ijkl} at temperature T but also with those at temperature T_q. Thus, the effectively needed input for the calculation of PDS and TDS are the elastic constants of the considered quasicrystal and the Bragg scattering intensities.

In order to keep computing time reasonable, $\Delta J(\mathbf{R}^*_\parallel+\mathbf{o}^*_\parallel)$ is calculated up to an offset $\mathbf{o}^*_\parallel$, which is set dynamical for each Bragg reflection. The maximal offset $\mathbf{o}^*_{\parallel,\max}$ for each reflection is chosen such that $\Delta J(\mathbf{R}^*_\parallel+\mathbf{o}^*_{\parallel,\max})\approx 0.0001\cdot\Delta J(\mathbf{R}^*_\parallel)$. This means that the calculated diffuse intensity at $\mathbf{o}^*_{\parallel,\max}$ for each reflection drops to about 0.0001 of

the diffuse intensity maximum in the pixel closest to the position of the corresponding Bragg reflection.

For the calculation of the Patterson function based on diffuse intensity data only, the diffuse scattering was *punched* around the location of each *measured* Bragg reflection by a small window function. For details on the *punch-and-fill* method refer to Part I of this study. In contrast to the punch function used in Part I (window function of size 9×9 pixels), the punch function used for the PDS and TDS calculation is 3×3 pixels only. Its influence in Patterson space is significant at Patterson vectors larger than 100 Å. In the case of the PDS and TDS calculation, the *punched* regions are not filled by the fill function, as it was done for the calculations in Part I. Although the Bragg reflections are not included, *punching* the diffuse diffraction pattern is necessary in the present case. Otherwise "numerical singularities," which are due to sampling effects of the PDS and TDS patterns, would control the Patterson maps (PM) of the diffuse scattering. Apparently, Eq. (1) shows a singularity at the position of each of the Bragg reflection: If $\mathbf{o}_{\parallel}^{*}$ approaches 0, $\Delta J(\mathbf{R}_{\parallel}^{*}+\mathbf{o}_{\parallel}^{*} \rightarrow 0)$ tends toward ∞. This is due to the fact that intensities are calculated on discrete pixel positions (∞ appears if a Bragg position falls exactly on a discrete pixel position). This is in contrast to the experiment, where the scattering information is integrated over the area of one pixel, which results in a finite value.

All following results of the PDS and TDS calculations are based on the theory of thermalized phonons and phasons. Only minor differences in the diffraction patterns and PMs can be observed in the case of quenched phasons. Chernikov *et al.*[44] has determined the full set of phononic elastic constants for a decagonal Al–Co–Ni quasicrystal with resonant ultrasound spectroscopy at ambient temperature. Thus, for a decagonal quasicrystal with point group $10/mmm$, one ends up with only four parameters for the thermalized case but still with 13 for the quenched case.

B. Dependence on the perpendicular-space component of diffraction vectors

What is the influence of a limitation of the perpendicular-space component of the diffraction vectors [see Eq. (16), Part I] on the diffuse scattering (PDS and TDS) and the corresponding Patterson function? PDS and TDS of a RPT is calculated for two datasets with a maximal parallel-space component of $d_{\parallel,\max}^{*}=2.5$ Å^{-1} and maximal perpendicular-space components of $d_{\perp,\max}^{*}=2$ Å^{-1} and $d_{\perp,\max}^{*}=5$ Å^{-1}, respectively. Zoomed sections of the calculated diffuse patterns are shown in Figs. 1(a) and 1(b), respectively, the corresponding PMs are depicted in Figs. 1(c) and 1(d). Note that all PMs depicted in this paper have been smoothed to minimize truncation effects from the Fourier transformation (see Part I for more details). All Bragg reflections stronger than 1 ppm of the intensity of the second strongest reflection are included in the calculations [$J(\mathbf{0})$ excluded]. This restriction gives a dataset comparable to what can be measured employing synchrotron radiation (dynamic range of $\approx 10^6$). In the case of $d_{\perp,\max}^{*}=2$ Å^{-1}, the datasets results in 17 300 Bragg reflections, in the case of $d_{\perp,\max}^{*}=5$ Å^{-1}, one obtains 98 350 reflections. The phononic elastic constants C_{ijkl} were taken from Chernikov,[44] the phasonic elastic constants were set to $K_1=0.02$, $K_4=0.4$ and the phonon-phason coupling constant to $R=0.1$. The diffraction patterns were calculated on a square grid of size 4001×4001 pixels.

Comparing the diffuse scattering of the two datasets [Figs. 1(a) and 1(b)], one can see a remarkable difference. The additional Bragg reflections in Fig. 1(b) evolve a streaklike pattern of diffuse scattering and clearly change the appearance of the whole pattern. Thus, streaklike diffuse scattering of quasicrystals may result from the superposition of PDS from the infinite number of unobservable weak Bragg reflections with high perpendicular-space components of the diffraction vectors. Note that for Bragg reflections with high perpendicular-space components, the corresponding PDS intensities may be by far stronger than the sharp Bragg intensities. Taking a closer look at the PMs of the two datasets [Figs. 1(c) and 1(d)] one can see hardly any difference between them. In particular for short Patterson vectors, both patterns look very similar. This corroborates the assumption, that the Patterson vectors in Figs. 1(c) and 1(d) originate from PDS and TDS and are not governed by perpendicular-space truncation errors.

C. Case studies

What is the influence of a variation of the elastic properties on the PDS and TDS calculations of a RPT? Five datasets with different elastic parameters are examined (see Table I). The number of sampling points is identical in all cases, namely, 4001×4001 pixels, as well as the maximal parallel-space component of $d_{\parallel,\max}^{*}=2.5$ Å^{-1} and the maximal perpendicular-space component $d_{\perp,\max}^{*}=2$ Å^{-1}. The case of pure PDS is realized by stiffening the RPT in parallel space, the case of pure TDS by stiffening it in perpendicular-space.

Zoomed sections of the diffraction patterns of the five cases are shown in Figs. 2(a)–2(e). The overall distribution of diffuse scattering looks very similar in cases (a)–(d) but differs from the case of pure TDS [Fig. 2(e)]. Usually, TDS is described by a function, which is zero at the origin of reciprocal space, then increases to a maximum that is roughly proportional to the square of the diffraction vector and finally decreases slowly because of the atomic factor [for details on TDS, see, e.g., Cowley[45]]. Note, that in the present study, TDS is calculated from a higher-dimensional approach developed within the framework of the hydrodynamic theory.[8–11] Although the overall distribution of the diffuse scattering in Figs. 2(a)–2(d) is very similar, the fine structure changes significantly.

As already mentioned in Sec. IV A, the influence of the *punch function* used for the PDS and TDS calculations is significant for Patterson vectors larger than 100 Å. Thus, reliable information on structural disorder can only be obtained for Patterson vectors up to 100 Å. Up to this distance, one can see hardly any difference between the PMs of the first four cases [Figs. 2(f)–2(i)]. As a consequence, the size of the plot has been limited to 30×30 Å. The striking similarity between the four PMs in Figs. 2(a)–2(d) can be explained with the distribution of low-frequency diffuse scattering in

TABLE I. Details on elastic constants for the PDS and TDS calculations. Units are in 10^{12} dyn/cm^2.

	$R>0$ Figs. 2(a) and 2(f)	$R=0$ Figs. 2(b) and 2(g)	$R<0$ Figs. 2(c) and 2(h)	pure PDS Figs. 2(d) and 2(i)	pure TDS Figs. 2(e) and 2(j)
C_{11}	2.34315	2.34315	2.34315	$1\cdot10^6$	2.34315
C_{13}	0.66625	0.66625	0.66625	$1\cdot10^6$	0.66625
C_{33}	2.32215	2.32215	2.32215	$1\cdot10^6$	2.32215
C_{44}	0.70190	0.70190	0.70190	$1\cdot10^6$	0.70190
C_{66}	0.88455	0.88455	0.88455	$1\cdot10^6$	0.88455
K_1	0.02	0.0189	0.0189	0.0189	$1\cdot10^6$
K_4	0.4	0.4	0.4	0.4	$1\cdot10^6$
R	0.1	0.0	−0.12	0.0	0.0

the respective diffraction patterns. Significant differences in Figs. 2(a)–2(d) can only be seen in the fine structure, this means in the high-frequency contributions to the diffuse scattering. Since high-frequency contributions in reciprocal space predominantly contribute to longer vectors in Patterson space, the similarity of the four PMs in Figs. 2(f)–2(i) is not surprising. Consequently, the influence of the fine structure of the diffuse scattering is significant at Patterson vectors larger than 100 Å. This has a great influence on investigations of local disorder phenomena from quasicrystals, which are due to phasonic disorder. Thus, the values for K_{ijkl} and R_{ijkl} may result quite arbitrarily from experimental studies. In contrast to the PMs of Figs. 2(f)–2(i), the Patterson function of TDS [Fig. 2(j)] shows uniformly distributed positive Patterson peaks, each with a negative "halo" around them. The absence of certain Patterson vectors in the PMs of the first four cases [see arrows in Figs. 2(f)–2(i)] means that the structure at these vectors corresponds to the average structure and thus, these vectors are not influenced by phasonic disorder. Consequently, the RPT is not uniformly disordered by phasons such as it is in the case of TDS. Note that the integrated diffuse intensity from the pure TDS case is at least one order of magnitude smaller than for the other cases.

V. MODELING PDS AND TDS BASED ON EXPERIMENTAL DATA

PDS and TDS is calculated based on synchrotron diffraction data of d-$Al_{71.5}Co_{14.6}Ni_{13.9}$ (see Sec. III for experimental details). The results are compared with the patterns of the *Edagawa phase* from Part I of our study. For best comparison, the data of d-$Al_{71.5}Co_{14.6}Ni_{13.9}$ has been matched in the following points to the ones from the *Edagawa phase*. The extent in reciprocal space is limited to ±0.8 Å^{-1}; the PMs are calculated from Bragg layers $\{hkl|-3\leqslant l\leqslant 3\}$ and calculations are performed on a square grid of size 2137 $\times$2137 pixels. The maximal perpendicular-space component of the d-$Al_{71.5}Co_{14.6}Ni_{13.9}$ data is $d^*_{\perp,\max}=2.5$ Å^{-1} and the elastic constants necessary for the PDS and TDS calculations are set equal to the ones in Sec. IV B. Again, all Bragg reflections stronger than 1 ppm of the intensity of the second strongest reflection are included in the calculations [$J(\mathbf{0})$ excluded].

Figures 3(a) and 3(d) show the *punched-and-filled* diffraction patterns at 1120 K from the *Edagawa phase* ($h_5=0$ and $h_5=2$, respectively, with index h_5 referring to the ≈8 Å superstructure). The original diffraction patterns are depicted in Figs. 3(b) and 3(e) and calculated PDS and TDS based on d-$Al_{71.5}Co_{14.6}Ni_{13.9}$ data in Figs. 3(c) and 3(f). Note that the *punched-and-filled* patterns [Figs. 3(a) and 3(d)] represent the extracted diffuse scattering from the original patterns [Figs. 3(b) and 3(e)] (for details on the *punch-and-fill* method, see Part I of our study). The calculated PDS and TDS patterns of d-$Al_{71.5}Co_{14.6}Ni_{13.9}$ show a good agreement with the overall distribution of diffuse scattering from the *Edagawa phase*. Differences are present in the fine structure of diffuse scattering (see zoomed sections) and in the diffuse streaks in the patterns of the *Edagawa phase*. These deviations are partly caused by the fact that not all reflections observable on the image plate patterns (*Edagawa phase*) have been measured by the single counter method (d-$Al_{71.5}Co_{14.6}Ni_{13.9}$). The diffuse streaks from the *Edagawa phase* connect main and $S1$ satellite reflections. No streaks can be observed between the different satellite reflections themselves, for example. This strong selection criterion cannot be met by the PDS and TDS calculations. These calculations are capable to produce diffuse streaks, but since no differentiation is made between the reflections, streaks are produced between all reflections among each other. Consequently, the PDS and TDS calculations are not capable to describe the diffuse streaks from the *Edagawa phase*. They appear to be of different origin. Nevertheless, the diffuse scattering differs mostly in the fine structure, i.e., high-frequency part of the scattering intensity, which hardly affects short Patterson vectors.

Figures 4(a), 4(c), and 4(e) shows the projected PM as well as the PMs at $z=0$ and $z=0.25$ of the *punched-and-filled* distribution of diffuse scattering from the *Edagawa phase* at 1120 K. The PMs of calculated PDS and TDS of the d-$Al_{71.5}Co_{14.6}Ni_{13.9}$ dataset are depicted in Figs. 4(b), 4(d), and 4(f), respectively. The correspondence between experiment and simulation is excellent. Consequently, structural disorder of the *Edagawa phase* for correlation lengths up to 60 Å can be described by phasonic disorder. The results do equally well when applied to the datasets collected at 300 and 1070 K but with the difference that the correlation lengths in these patterns are smaller (see Part I of our study).

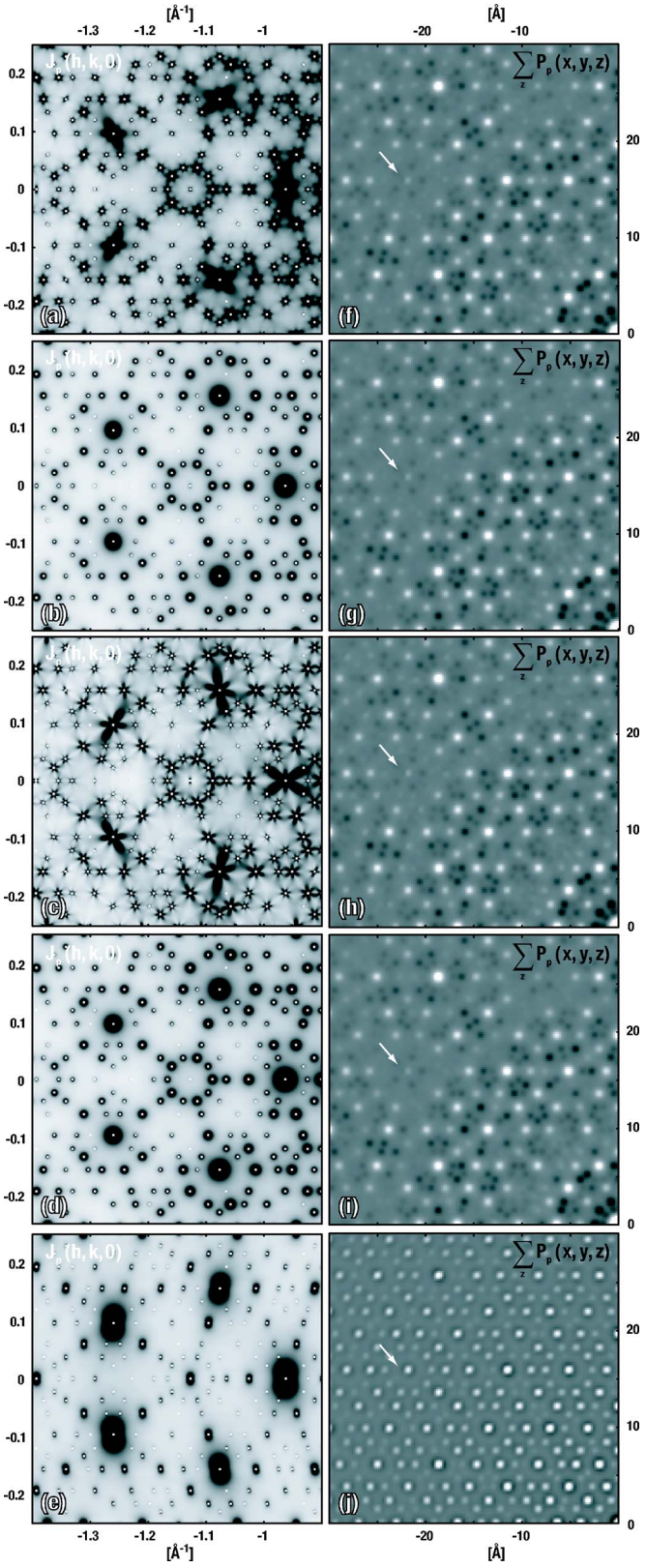

FIG. 2. Influence of a variation of the elastic parameters on the PDS and TDS calculations of a RPT in reciprocal and Patterson space (see Table I). Zoomed sections of the diffraction patterns of the five cases examined are shown in (a)–(e), the corresponding PMs in (f)–(j). The overall distribution of diffuse scattering looks very similar in the cases (a)–(d) but the fine structure changes significantly. Hardly any differences can be observed in the PMs of the first four cases (f)–(i). Arrows indicate absent Patterson vectors in the cases (f)–(i). Relative scaling of the intensities in the patterns (f)–(j) is 80:40:160:40:1.

Note that the accessible region in the PMs of the *Edagawa phase* extends to about 60 Å (see Part I of our study). Beyond this limit, information on the difference structure is no more accessible by our dataset and the *punch-and-fill* method. Noticeable differences between experiment and simulation can only be observed in the PMs at $z=0.25$. There, the *punched-and-filled* PM of the *Edagawa phase* shows additional positive Patterson peaks with regard to the PM of PDS and TDS [see arrows in Figs. 4(e) and 4(f)]. These peaks may be due to disorder phenomena of the *Eda-*

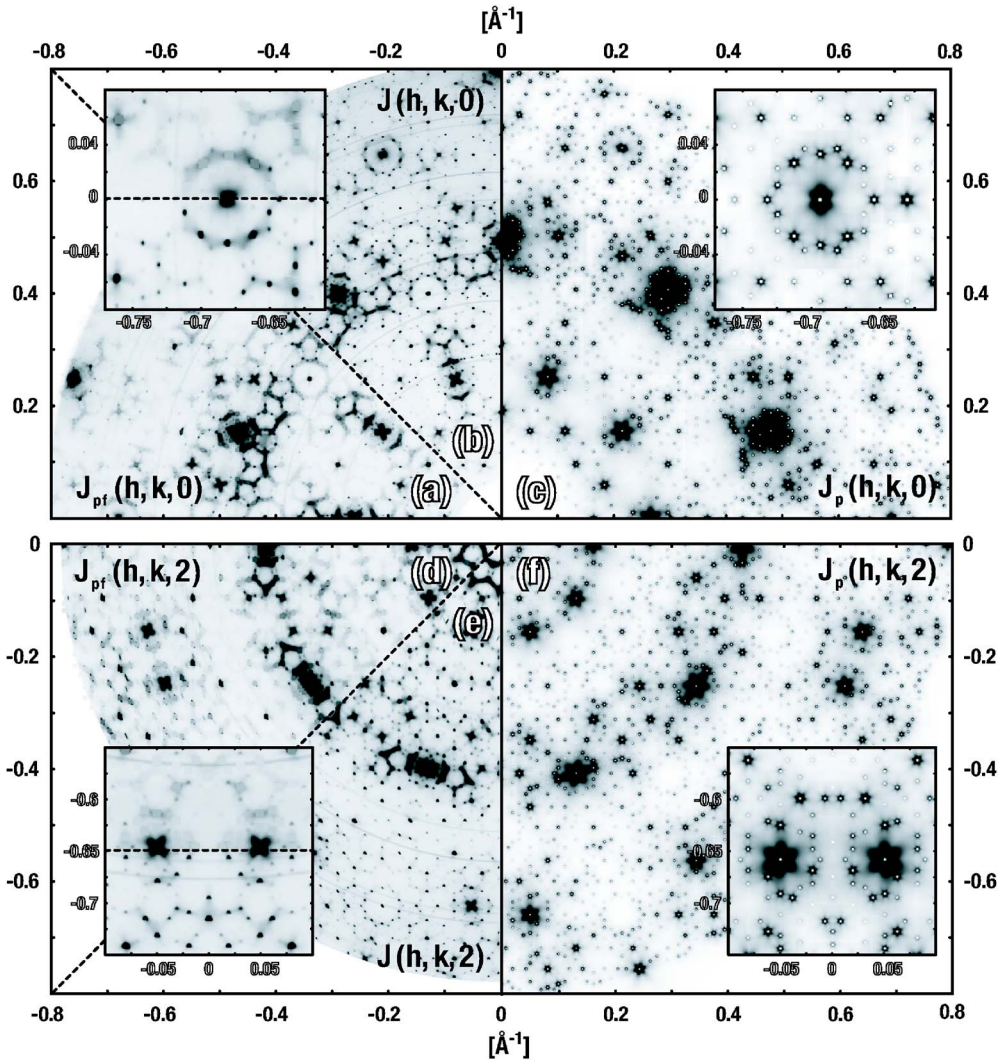

FIG. 3. Comparison of experimental and calculated diffraction patterns. (a) and (d) show the *punched-and-filled* diffraction patterns at 1120 K from the *Edagawa phase* (Ref. 7) at $h_5=0$ and $h_5=2$, respectively, (b) and (e) the original diffraction patterns, and (c) and (f) calculated PDS and TDS of the *d*-$Al_{71.5}Co_{14.6}Ni_{13.9}$ dataset. Zoomed sections in the insets show differences between the experimental and calculated patterns. The index h_5 refers to the $\approx$8 Å superstructure.

gawa phase, which are not described by phasonic disorder or due to some structural differences between *d*-$Al_{71.5}Co_{14.6}Ni_{13.9}$ (single counter data) and *d*-$Al_{70}Co_{12}Ni_{18}$ (image plate data).

VI. MODELING DISORDER ON THE SCALE OF CLUSTERS

In the following calculations of structural disorder phenomena, a Patterson function approach is used, in which correlations *between* structural building units (e.g., clusters) are ignored. As a consequence, intercluster Patterson vectors from the disordered structure are the same as the corresponding intercluster Patterson vectors from the average structure. Thus, the Patterson function from the difference structure only shows intracluster Patterson vectors. Consequently, the structural model can be limited to the size of a single columnar cluster. This approach is described in more detail by Cowley.[45]

Given a number m of different cluster configurations, the diffuse intensity may then be written in the form

$$I_{\text{diffuse}}(\mathbf{r}^*) = \frac{1}{m}\sum_{i=1}^{m} |F_i(\mathbf{r}^*) - F_{\text{aver}}(\mathbf{r}^*)|^2, \qquad (2)$$

as long as the probabilities for each cluster configuration m is the same. $F_i(\mathbf{r}^*)$ are the Fourier transforms of $\rho_i(\mathbf{r})$, which represent the electron density distributions of the different cluster configurations. In all the following calculations of local disorder phenomena, the diffuse scattering resulting from a specific disorder phenomenon has been calculated according to Eq. (2). Note that since no intercluster correlations are included in the approach, the PMs calculated therefrom do not show Patterson vectors longer than the diameter of a single columnar cluster.

Various kinds of disorder phenomena of about 20–32 Å-sized clusters have been simulated with the goal to

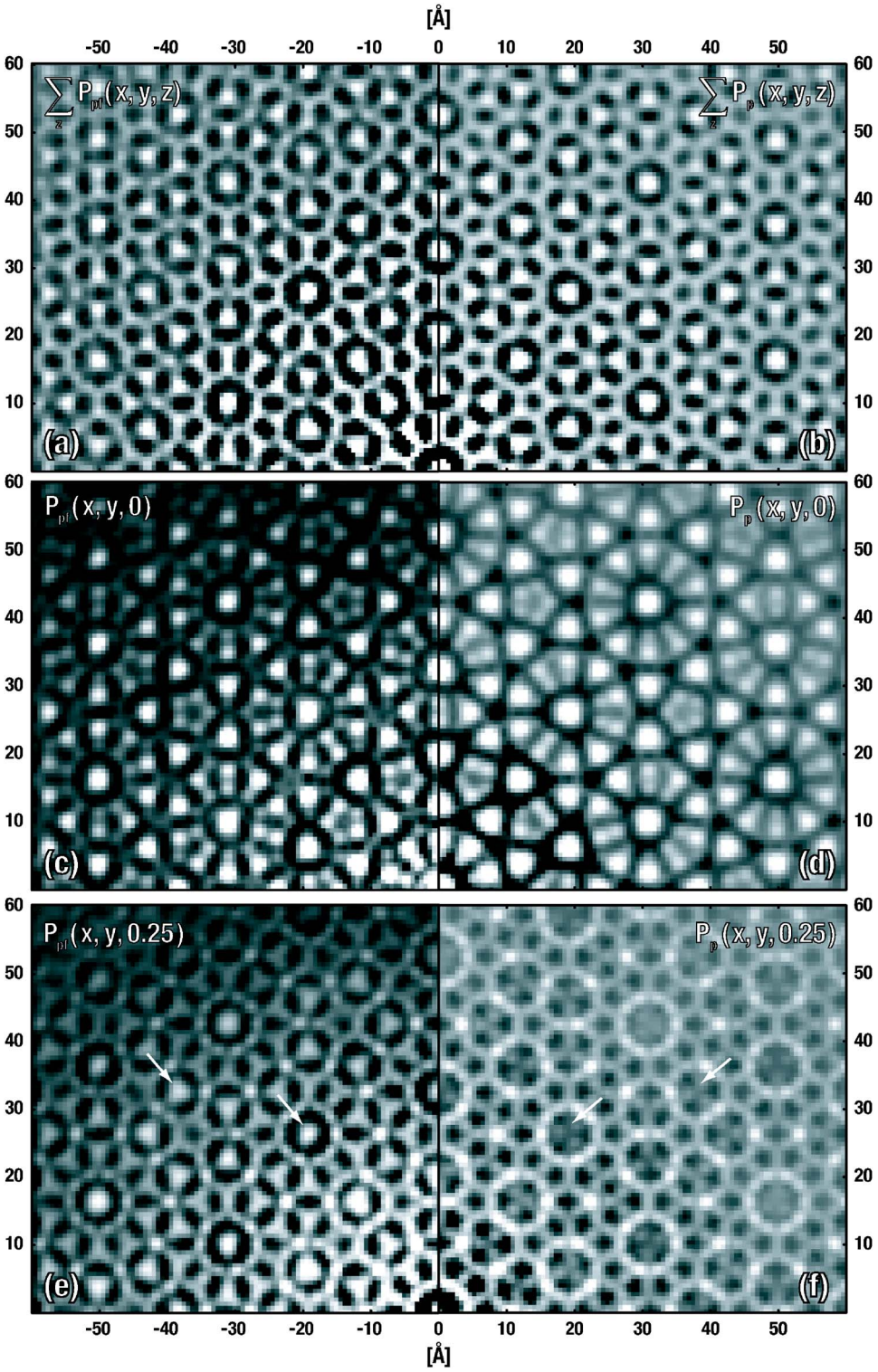

FIG. 4. Projected PM (a), the PMs at $z=0$ (c) and $z=0.25$ (e) of the *punched-and-filled* distribution of diffuse scattering from the Edagawa phase at 1120 K in comparison with the Patterson function of calculated PDS and TDS of the d-$Al_{71.5}Co_{14.6}Ni_{13.9}$ dataset (b), (d), and (f), respectively. The *punched-and-filled* PM of the *Edagawa phase* shows additional positive Patterson peaks with regard to the PM of PDS and TDS [see arrows in (e) and (f)]. Relative scaling of the intensities in the patterns (a), (c), and (e) is 1:10:10 and in (b), (d), and (f) it is 1:5:10.

identify local disorder phenomena of clusters and their subunits. We have investigated the following models of disorder: substitutional disorder between TM and Al; occupational disorder of Al; displacive disorder of whole clusters along the periodic axis with displacements of 2 and 4 Å; different local environments around Co and Ni; orientational disorder of clusters or subunits therein; size-effect like distortions between Co and Ni; and also combinations of these disorder phenomena. The simulations have been performed on the most reasonable cluster models reported in literature (see Sec. II B). Due to the lack of cluster models for the *Edagawa phase* (four-layer structure), we predominantly used two-layer structure models to model disorder phenomena, which describe the diffuse intensities inside the Bragg layers of the *Edagawa phase*. Thus, the two-layer cluster must result from the projection of the four-layer structure with sequence A, B, A', B' onto a two-layer structure with sequence $(A+A')$, $(B+B')$. This projection allows the use of two-layer cluster

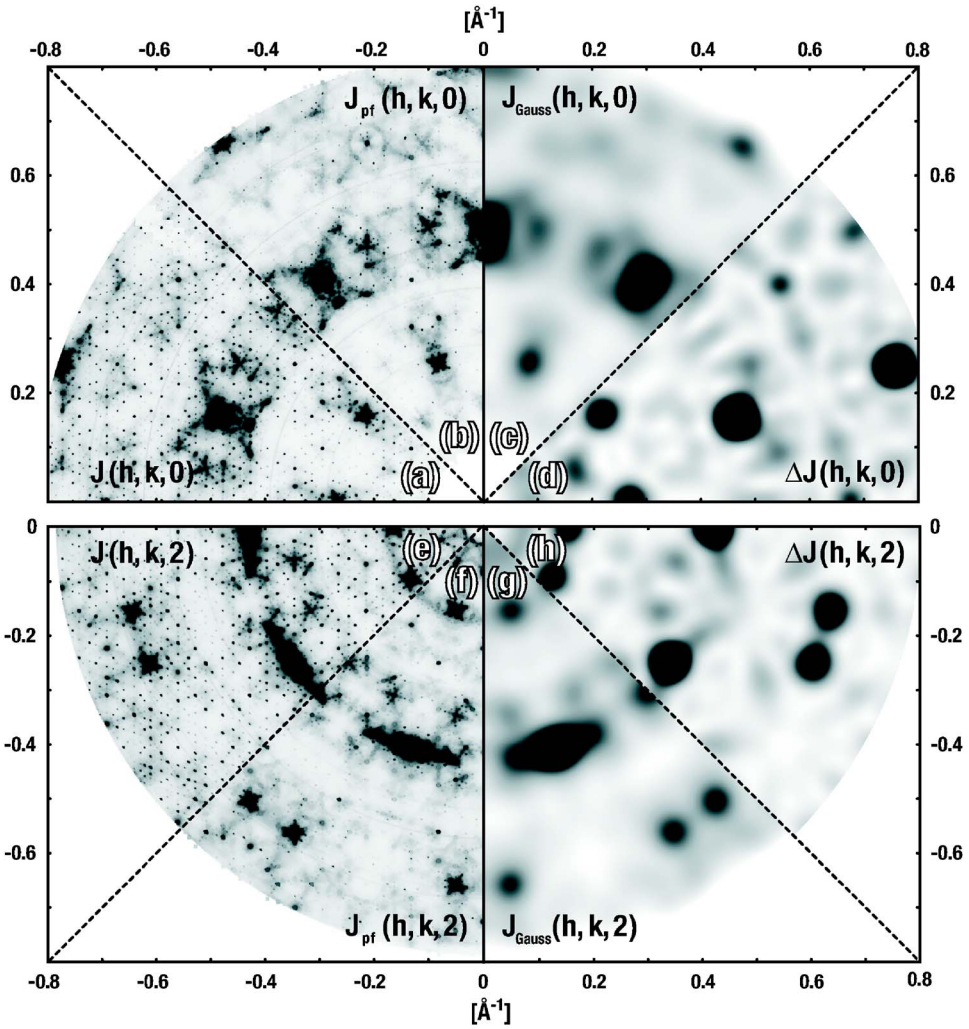

FIG. 5. Comparison of experimental and calculated diffraction patterns. (a), (e) show the original diffraction patterns at 300 K from the *Edagawa phase* at $h_5=0$ and $h_5=2$, respectively, (b) and (f) the *punched-and-filled* diffraction patterns, (c) and (g) the filtered diffraction pattern, and (d) and (h) calculated diffuse scattering from fivefold orientational disorder of the Abe cluster. Note that the size of the cluster ($\approx$20 Å in diameter) limits the smallest width of a calculated diffuse feature to about 0.05 Å^{-1}.

models, which are chemically not reasonable, e.g., have too short atomic distances or atomic sites with mixed occupancy in contrast to the underlying four-layer model.

Best results are obtained with the cluster-model of Abe *et al.*[24] It shows mirror symmetry and a pseudo 10_5-screw axis along the periodic axis (rotation of 180° and translation of $\approx$2 Å). The latter symmetry operator is fulfilled by a bigger part of the cluster, although disagreement is present in the central part of the cluster and the *P* subclusters,[30] which are subunits of the Abe cluster.

Best agreement between the experimental diffraction patterns of the *Edagawa phase* from Part I and calculated diffuse scattering is obtained for a fivefold orientationally disordered Abe cluster.[24] For the best comparison, the data of the present calculations have been matched to the ones from the *Edagawa phase*, as described in Sec. V. Figures 5(a) and 5(e) show the original diffraction patterns at 300 K of the *Edagawa phase* ($h_5=0$ and $h_5=2$, respectively). The *punched-and-filled* diffraction patterns are depicted in Figs. 5(b) and 5(f), the filtered diffraction patterns in Figs. 5(c) and 5(g) and calculated diffuse scattering from fivefold orientational disorder of the Abe cluster is shown in Figs. 5(d) and 5(h). Filtering of the patterns in Figs. 5(c) and 5(g) was done in Patterson space by multiplying the PMs from the *punched-and-filled* diffraction patterns with a two-dimensional Gaussian function (maximum at the origin, 2σ at 21 Å). The calculated diffuse scattering is in good agreement with the overall distribution of diffuse scattering from the *Edagawa phase*, both at $h_5=0$ and $h_5=2$ [Fig. 5(d) compared to Fig. 5(c) and Fig. 5(h) compared to Fig. 5(g)]. Note, that the size of the cluster ($\approx$20 Å) in diameter) limits the smallest width of a calculated diffuse feature to about 0.05 Å^{-1}. The application of fivefold orientational disorder on clusters with 5*m* symmetry, like the clusters proposed by Hiraga *et al.*[25–27] and Ritsch *et al.*,[28,29] does not produce any diffuse scattering at all.

Figures 6(a), 6(c), and 6(e) shows the projected PM as well as the PMs at $z=0$ and $z=0.25$ of the *punched-and-filled* distribution of diffuse scattering from the *Edagawa phase* at 300 K. The Patterson function of calculated diffuse scattering from the fivefold orientationally disordered Abe cluster is depicted in Figs. 6(b), 6(d), and 6(f). The correspondence between experiment and simulation is very good, although minor differences can be spotted in the PMs. These results do equally well apply to the datasets collected at 1070 and 1120 K of the *Edagawa phase*. As described in the previous paragraph, the Patterson function of calculated diffuse scattering does only extend up to Patterson vectors close to 20 Å (diameter of a cluster). Note that the PMs (up to $\approx$20 Å) of diffuse scattering from the *Edagawa phase* are almost

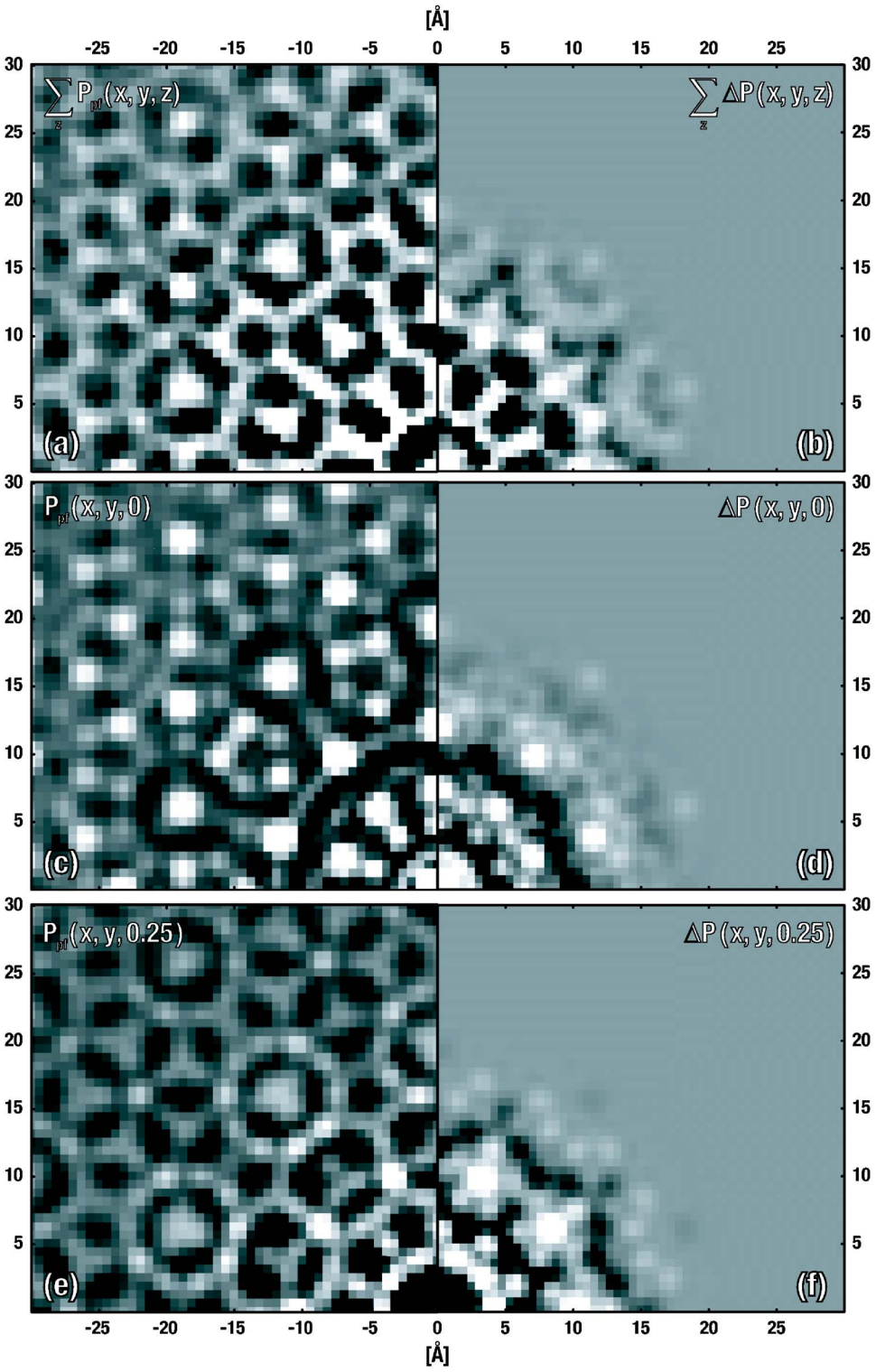

FIG. 6. Projected PM (a), the PMs at $z=0$ (c) and $z=0.25$ (e) of the *punched-and-filled* distribution of diffuse scattering from the *Edagawa phase* at 300 K in comparison with the Patterson function of calculated diffuse scattering from the fivefold orientationally disordered Abe cluster (b), (d), and (f), respectively. Relative scaling of the intensities in the patterns (a), (c), and (e) is 1:10:10 and in (b), (d), and (f) it is 1:3:3.

equally well described by PDS or fivefold orientational disorder of the Abe cluster [compare Figs. 4 and 6]. This is a strong indication that fivefold orientational disorder of clusters is the short-range 3D structural representation of 5D phasonic disorder. Orientational disorder of clusters can be induced by phasons as will be shown in an upcoming section.

Fivefold orientational disorder of the Abe cluster produces several local disorder phenomena, which are illustrated in Fig. 7. These are flips of Al atoms on a scale of ≈ 1 Å (label 1), substitutional disorder between TM and Al (label 2), occupational disorder of TM or Al (label 3, 4) and split positions between TM and Al (label 5). The pentagons in the center of layers *A* (label 6) and *B* (label 7) differ in orientation by 36° and have a different chemical composition. The pentagon in layer *A* contains only TM atoms, whereas the pentagon in layer *B* is composed both of TM and Al. The former pentagon would give only little contrast variation in

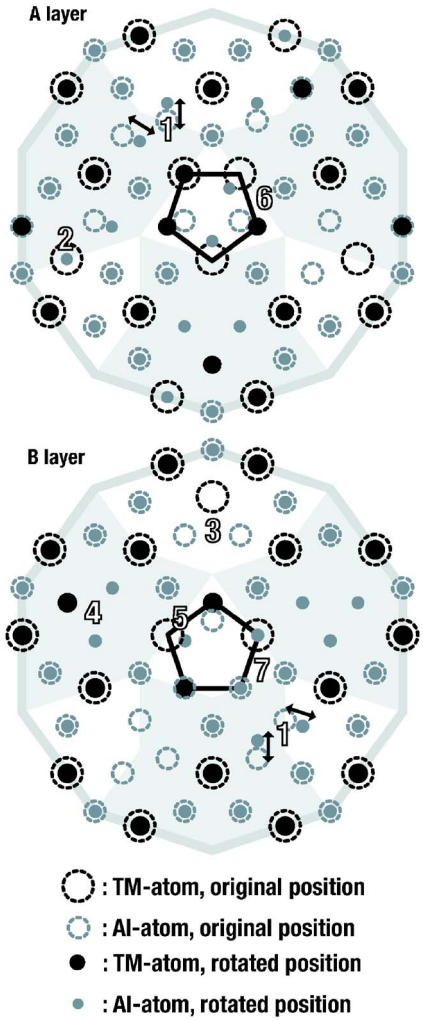

FIG. 7. Local disorder phenomena induced in the Abe cluster by a rotation of 72°. The upper part shows the effects on the *A* layer, the lower part on the *B* layer. Observable local disorder phenomena are flips of Al atoms (label 1), substitutional disorder between TM and Al (label 2), occupational disorder of TM or Al (labels 3 and 4) and split positions between TM and Al (label 5). The pentagons in the center of layer *A* (label 6) and *B* (label 7) differ in orientation by 36° and have a different chemical composition.

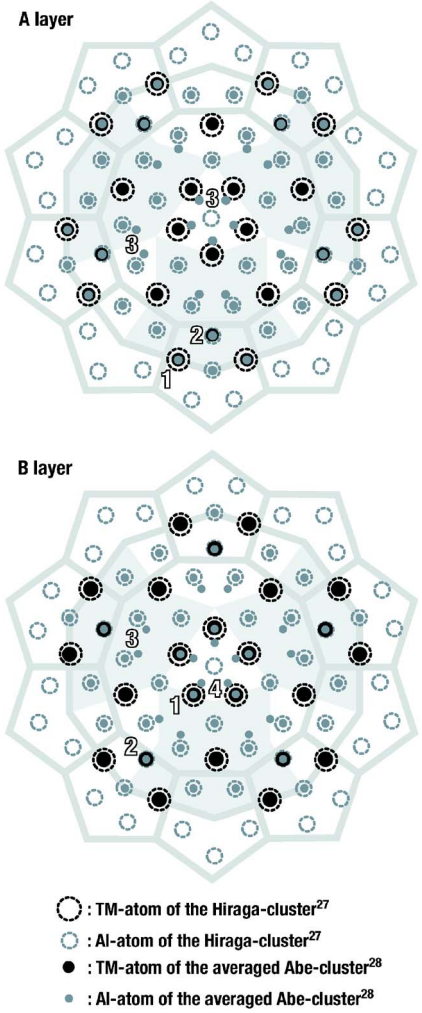

FIG. 8. A superposition of the Hiraga-cluster (Ref. 27) and the average structure of the fivefold orientationally disordered Abe cluster (Ref. 24). The Hiraga cluster has 5*m* symmetry, while the original Abe cluster shows mirror symmetry only. Almost all atomic sites of the Hiraga cluster coincide with the atomic sites of the averaged Abe cluster. The averaged Abe cluster shows mixed TM/Al occupancy, while the Hiraga cluster contains either TM (label 1) or Al (label 2). Furthermore, the averaged Abe cluster shows Al split positions (label 3) and split positions between mixed atomic sites and Al (label 4).

high-resolution transmission electron microscopy (HRTEM) images whereby the latter would show pseudofivefold symmetry. Fivefold orientational disorder of the Abe cluster has also some remarkable consequences on the symmetry of the cluster. Not only does the symmetry of the average cluster increase from *m* to 5*m*, but also the pseudo-10_5-screw axis turns almost into a real 10_5-screw axis. These observations are partly in accordance with the findings of Hiraga *et al.*,[27] who described the average cluster of the Ni-rich basic phase by a ≈32 Å cluster having 5*m* symmetry and a 10_5-screw axis along the periodic direction.

VII. DISCUSSION

A. Cluster symmetry

EM studies on decagonal Al–Co–Ni quasicrystals significantly differ in the symmetry of the fundamental columnar clusters derived from them. Cluster models having mirror symmetry compete against cluster models showing 5*m* symmetry. Possibly, fivefold orientational disorder plays an important role in the appearance of symmetry on HRTEM or high-angle annular dark-field scanning transmission electron microscopy (HAADF-STEM) images. HRTEM and HAADF-STEM are techniques, in which time and space averaging takes place over different scales. If we assume that the real cluster possesses mirror symmetry, then the average structure of the fivefold orientationally disordered cluster would have 5*m* symmetry. How this could look like is illustrated schematically in Fig. 8, which shows a superposition of the Hiraga cluster[27] and the average structure of the fivefold orientationally disordered Abe cluster.[24] Both models are used to describe the structure of the Ni-rich basic phase.

The agreement between the two models is remarkable. Almost all atomic sites of the Hiraga cluster coincide with the atomic sites of the averaged Abe cluster. Nevertheless, minor differences between both models can be found. The averaged Abe cluster shows mixed TM/Al occupancy, while the Hiraga cluster contains either TM [Fig. 8, label 1] or Al (label 2). Furthermore, the averaged Abe cluster shows Al split positions (label 3) and split positions between mixed atomic sites and Al (label 4). Note that the averaged Abe cluster shows a 10_5-screw axis, while the not averaged cluster possesses a pseudo-10_5-screw axis only.

B. 3D structural representation of PDS

How can PDS, which is well defined in five-dimensional space, be described in three dimensions? This question is a central topic in diffuse scattering studies of quasicrystals, which has not yet been satisfactorily answered. We show that PDS produces local disorder phenomena, which can equivalently be described by a fivefold orientational disorder of clusters (up to the diameter of a columnar cluster). Model calculations using only main reflections from the complete d-$Al_{71.5}Co_{14.6}Ni_{13.9}$ dataset (extent in reciprocal-space up to ± 1.5 Å^{-1}, the PMs are calculated from Bragg layers $\{hkl | -6 \leqslant l \leqslant 6\}$) are compared with results from fivefold orientational disorder of the Abe cluster[24] (same constraints as above). The large extent in reciprocal space results in an atomic resolution (≈ 1 Å) of the difference PMs. This corresponds almost to the doubled resolution (≈ 2 Å) of the PMs depicted in Figs. 4 and 6. All calculations have been performed on a square grid of size 2401×2401 pixels and the elastic constants for the PDS and TDS calculations are equal to the ones described in Sec. IV B.

Figures 9(a), 9(c), and 9(e) show the projected PM as well as the PMs at $z=0$ and $z=0.25$ of the average structure of d-$Al_{71.5}Co_{14.6}Ni_{13.9}$. The Patterson function of the average structure of the fivefold orientationally disordered Abe cluster is depicted in Figs. 9(b), 9(d), and 9(f), respectively. The PMs of the average structure of d-$Al_{71.5}Co_{14.6}Ni_{13.9}$ have been calculated by Fourier transformation of the corresponding reciprocal layers, which have been generated by convoluting the Bragg reflections with two-dimensional Gaussian functions. This procedure is necessary, since the Bragg patterns, which consist of δ functions with Laue symmetry $10/mmm$, cannot otherwise be mapped on a quadratic grid. The agreement between the patterns is excellent indicating that the local average structure of d-$Al_{71.5}Co_{14.6}Ni_{13.9}$ corresponds to the average structure of the fivefold orientationally disordered Abe cluster. Note that the Abe cluster has been derived from EM investigations, from which one only obtains the projected structure. Thus, information like the patterns in Figs. 9(c)–9(f) are not directly accessible by EM investigations. Good agreement with the PMs of the average structure of d-$Al_{71.5}Co_{14.6}Ni_{13.9}$ has also been obtained by computing the average structures of fivefold orientationally disordered clusters of Abe *et al.*,[23] Steinhardt *et al.*,[31,32] Yan *et al.*,[35] Yan and Pennycook,[36–38] and Hiraga *et al.*[27] Nevertheless, a better agreement was obtained with the cluster of Abe *et al.*[24]

Figures 10(a), 10(c), and 10(e) shows the projected PM as well as the PMs at $z=0$ and $z=0.25$ of calculated PDS and TDS from the d-$Al_{71.5}Co_{14.6}Ni_{13.9}$ dataset. They are compared with the PMs of diffuse scattering resulting from the fivefold orientationally disordered Abe cluster [Figs. 10(b), 10(d), and 10(f)], respectively. Excellent agreement between the two models of disorder is obtained. The difference structure of the fivefold orientationally disordered Abe cluster clearly corresponds to the local difference structure of the 3D description of phasonic disorder of d-$Al_{71.5}Co_{14.6}Ni_{13.9}$. Concerning the clusters of Abe *et al.*,[23] Steinhardt *et al.*,[31,32] Yan *et al.*,[35] and Yan and Pennycook,[36–38] the agreement of the difference PMs is less distinct than for the cluster of Abe *et al.*,[24] but still good. The cluster of Hiraga *et al.*[27] does not show any diffuse scattering caused by a fivefold orientational disorder, because of its symmetry. These observations indicate that PDS in decagonal quasicrystals can generally be described as fivefold orientational disorder of clusters. In the present study, this has been shown for decagonal quasicrystals, the quasiperiodic patterns of which may be described by a RPT and the clusters of which are mirror symmetric. Nothing can be said for other types of quasicrystals.

C. Average structure modifications induced by phasonic fluctuations

What kind of influence do phasons and phonons have on the higher-dimensional description of quasicrystals? Phonons in normal crystals smear out the probability density of atoms in the average structure. In quasicrystals their influence is similar, but here phonons broaden the ASs only in parallel space, which leads to displacive disorder in the cut space. By cut space we mean the atomic configurations in parallel space, which are obtained through a cut of the higher-dimensional embedding space by the parallel space. Phasons are responsible for the broadening of the ASs in perpendicular space, which causes substitutional disorder and split positions in the cut space. The phonon-phason coupling term couples phasonic and phononic fluctuations of the ASs. Consequently, in the case of a strong coupling term, phononic fluctuations induce phasonic disorder and *vice versa*. An interesting question concerns the modifications that the average structure in the cut space undergoes if phasonic fluctuations of the ASs are introduced.

To answer this question we have constructed RPTs (as described in Sec. IV) with slightly different radii of the ASs. The radii of the six considered cases are the following: $\{(0.36+i\cdot 0.04)\cdot a/\tau^2 | i=0,1,2,3,4,5\}$ and $\{(0.36+i\cdot 0.04)\cdot a/\tau | i=0,1,2,3,4,5\}$ for the ASs at $p=1,4$ and at $p=2,3$, respectively. A RPT in the standard embedding has ASs with radii $0.4\cdot a/\tau^2$ and $0.4\cdot a/\tau$, respectively. The cut spaces of the six cases are shown in Figs. 11(a)–11(f), respectively. The average structure of the highlighted cluster changes significantly with increasing radii of the ASs, i.e., increasing amount of phasonic disorder. Note that the considered datasets are cutouts of 5D infinite lattices. This fact leads to perpendicular-space truncation errors, which give rise to additional atomic positions in the cut spaces of Figs. 11(a)–11(f). The structure in (a) is well described by a

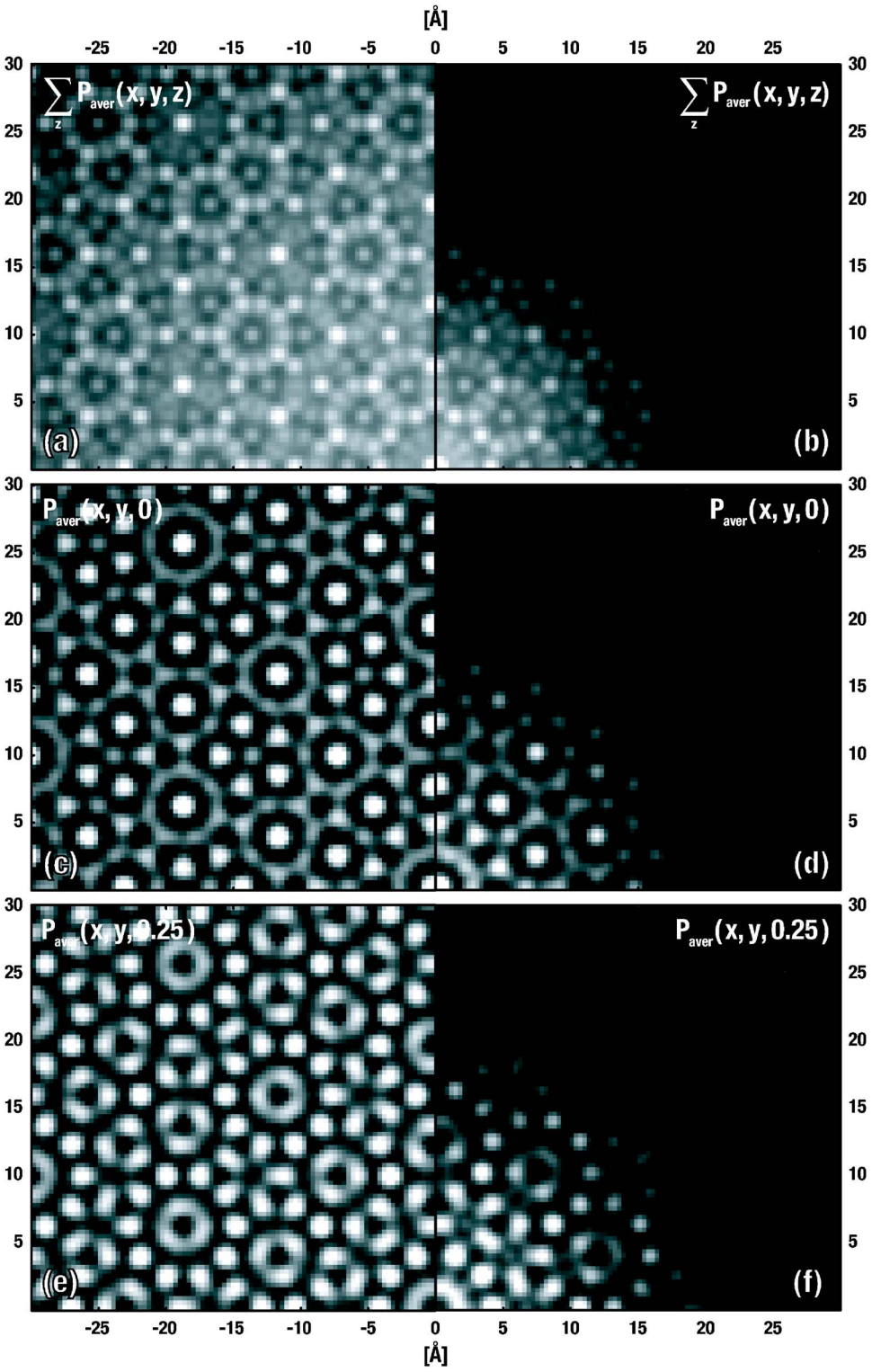

FIG. 9. Projected PM (a), the PMs at $z=0$ (c) and $z=0.25$ (e) of the average structure of the *d*-$Al_{71.5}Co_{14.6}Ni_{13.9}$ dataset calculated from main reflections in comparison with the Patterson function of the average structure of the fivefold orientationally disordered Abe cluster (b), (d), (f), respectively. The local average structure of *d*-$Al_{71.5}Co_{14.6}Ni_{13.9}$ corresponds to the average structure of the fivefold orientationally disordered Abe cluster. Relative scaling of the intensities in the patterns (a), (c), and (e) is 1:2:2 and in (b), (d), and (f) it is 1:4:3.

hexagon-boat-star tiling (HBS), while the structure in (b) follows an idealized tie-and-navette tiling. Closer inspection of the highlighted cluster in (c) reveals an ordering, which can be described by a fivefold orientational disorder of the cluster from (a). Further increase of the ASs leads to an increasing number of clusters, which are best described by fivefold orientational disorder (d)–(f). Thus, the formation of average clusters, which correspond to fivefold orientationally disordered clusters, naturally evolves by introducing phasonic fluctuations of the ASs, i.e., phasons induce orientational disorder of clusters.

D. Structural disorder of the quasiperiodic superstructure

The structure of the quasiperiodic superstructure of the *Edagawa phase* is still an unsolved question. Several models based on EM studies have been proposed. They have some kind of ordering between the fundamental columnar clusters

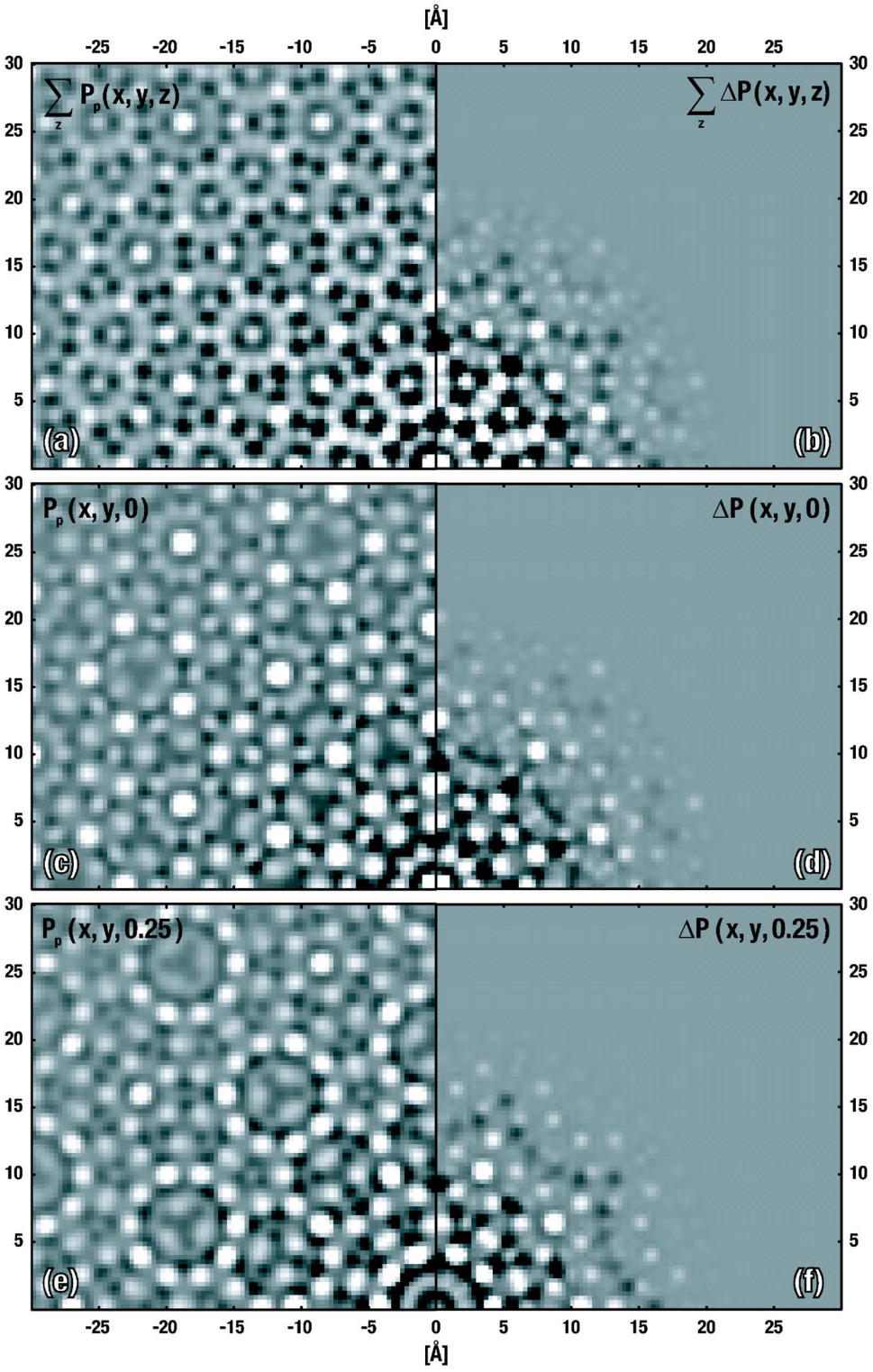

FIG. 10. Projected PM (a), the PMs at $z=0$ (c) and $z=0.25$ (e) of calculated PDS and TDS of the d-$Al_{71.5}Co_{14.6}Ni_{13.9}$ dataset calculated from main reflections in comparison with the Patterson function of calculated diffuse scattering from the fivefold orientationally disordered Abe cluster (b), (d), and (f), respectively. The difference structure of the fivefold orientationally disordered Abe cluster corresponds to the local difference structure of phason disordered d-$Al_{71.5}Co_{14.6}Ni_{13.9}$. Relative scaling of the intensities in the patterns (a), (c), and (e) is 1:3:3 and in (b), (d), and (f) it is 1:5:6.

in common.[46,47] None of the studies published so far deal with the structural disorder associated with the superstructure ordering. Our calculations of PDS and TDS based on the d-$Al_{71.5}Co_{14.6}Ni_{13.9}$ dataset (including main and satellite reflections) in Sec. V have shown good agreement with the PMs of the *Edagawa phase*. On the basis of these calculations we studied the structural disorder associated with the superstructure ordering only.

PDS and TDS is calculated based on $S1$ and $S2$ satellite reflections of the complete d-$Al_{71.5}Co_{14.6}Ni_{13.9}$ dataset (extent in reciprocal-space up to ± 1.5 Å^{-1}, the PMs are calculated from Bragg layers $\{hkl|-6 \leqslant l \leqslant 6\}$). All calculations have been performed on a square grid of size 2401 $\times$2401 pixels with elastic constants for the PDS and TDS calculations equal to the ones in Sec. IV B. Figures 12(a), 12(c), and 12(e) show the projected PM as well as the PMs at

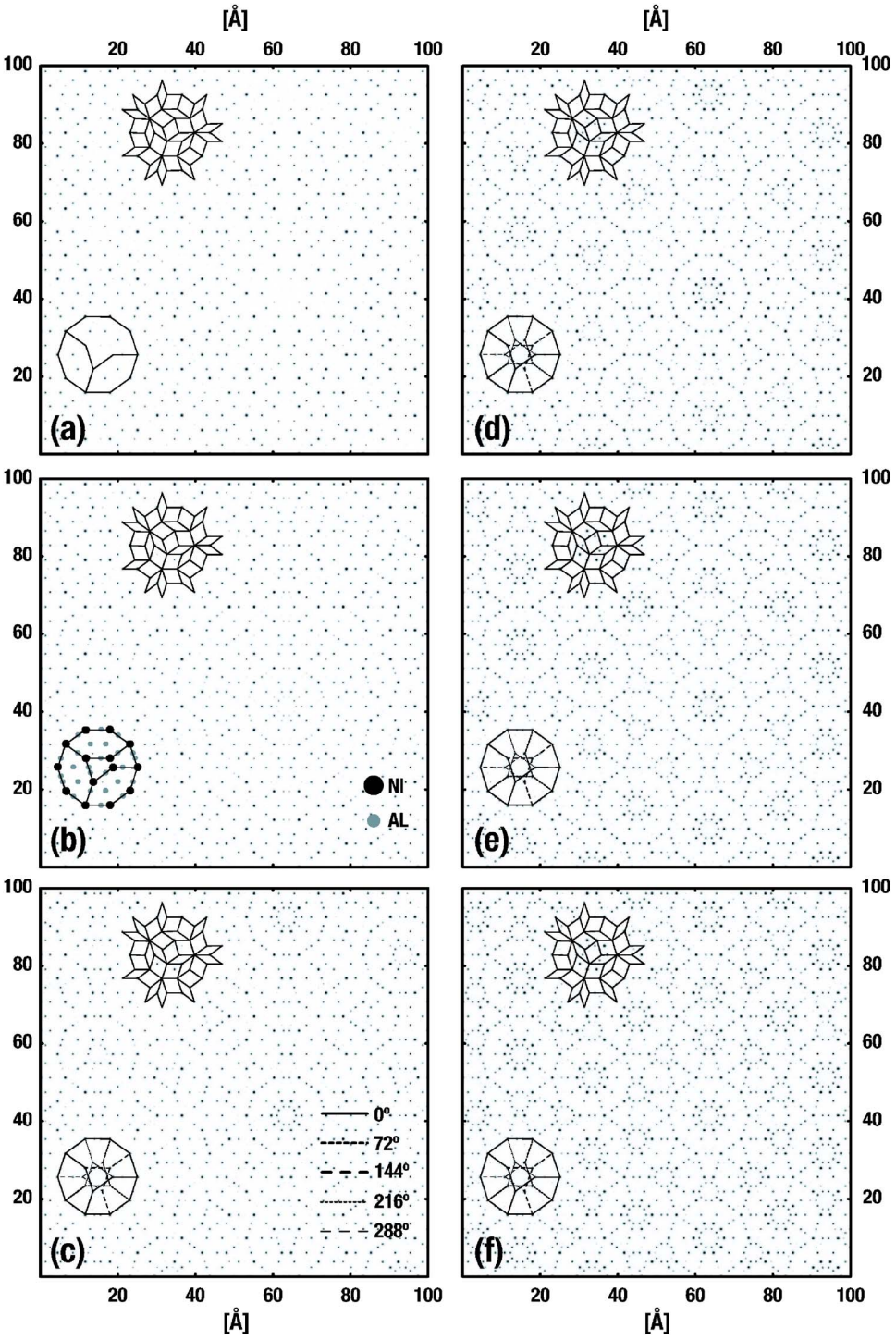

FIG. 11. Influence of phasonic fluctuations of the ASs of a RPT on the atomic configurations in parallel space (modeled by radii fluctuations of the ASs). The average structures with increasing radii are shown in (a)–(f), respectively. The structure in (a) is well described by a hexagon-boat-star tiling, while the structure in (b) follows an idealized tie-and-navette tiling. The structure in (c) can be described by fivefold orientational disorder of the cluster from (a). Further increase of the ASs leads to an increasing number of clusters, which are best described by fivefold orientationally disordered clusters (d)–(f). A small section of the underlying RPT is depicted in (a)–(f).

$z=0$ and $z=0.25$ of PDS and TDS calculated only from $S1$ reflections of the d-$Al_{71.5}Co_{14.6}Ni_{13.9}$ dataset. They are compared with the difference PMs calculated from the $S2$ reflections only Figs. 12(b), 12(d), and 12(f), respectively. The PMs show a correspondence between maxima in one pattern and minima in the other pattern [see arrows in Figs. 12(a)–12(d). As described in Part I, these strong Patterson peaks may be related to translation vectors, which correspond to intercluster vectors between centers of the *Gummelt* decagons in the corresponding quasiperiodic covering. The fine structure around these Patterson peaks is due to intercluster correlations. The projected PM of the $S2$ reflections is strongly structured, indicating the presence of both intra- and intercluster correlations, whereas the pattern of the $S1$ reflections mainly shows intercluster correlations. The correlations inside quasiperiodic planes of $S1$ and $S2$ reflections show similar correlation lengths of the underlying disorder phenomena [Figs. 12(c) and 12(d)]. However, the correlations between adjacent quasiperiodic layers [Figs. 12(e) and 12(f)] show a remarkable difference in the pattern of the $S1$ and $S2$ reflections. The PM at $z=0.25$ calculated from $S1$ reflections does hardly show any correlations in contrast to the pattern

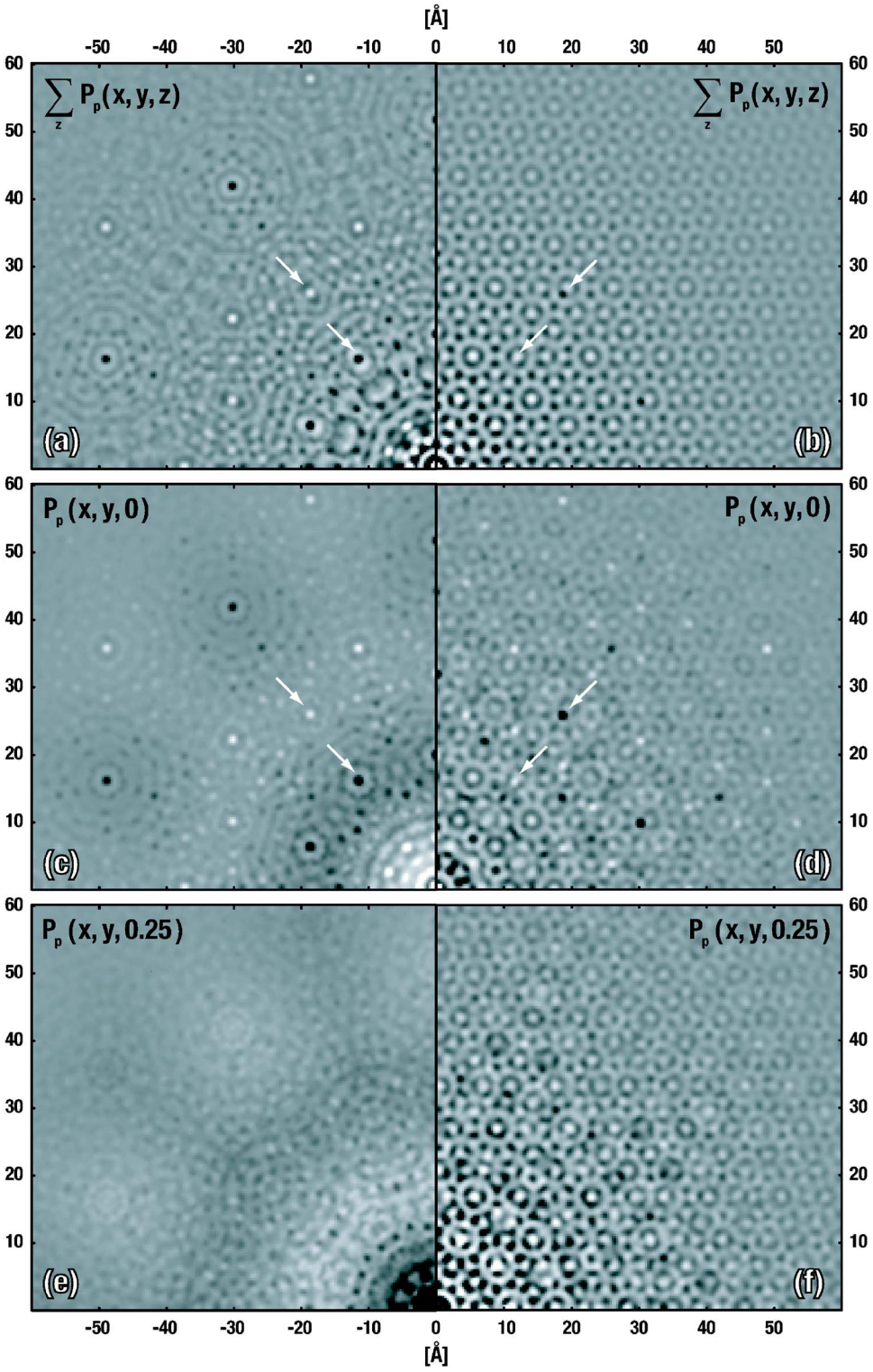

FIG. 12. Projected PM (a), the PMs at $z=0$ (c) and $z=0.25$ (e) of PDS and TDS calculated from $S1$ reflections [indexing after Edagawa *et al.* (Ref. 7)] of the *d*-$Al_{71.5}Co_{14.6}Ni_{13.9}$ dataset in comparison with PMs calculated from $S2$ reflections (b), (d), and (f), respectively. Strong maxima in one pattern often correspond to minima in the other pattern (see arrows). (b) is strongly structured, indicating the presence of both intra- and intercluster correlations, whereby (a) mainly shows intercluster correlations. Correlations between adjacent quasiperiodic layers (e), (f) differ significantly. (e) shows hardly any correlations in contrast to the (f) which is strongly structured both at small and long Patterson vectors. Relative scaling of the intensities in the patterns (a)–(f) is 5:5:70:20:50:8.

of the $S2$ reflections. The latter shows a strongly structured pattern both at small and long Patterson vectors. Note that the $S1$ and $S2$ reflections of the *Edagawa phase* exhibit a different temperature dependence, as reported in Part I. In a certain temperature range, the intensities of $S1$ reflections decrease with increasing temperature, while those of $S2$ reflections increase. Streaks interconnecting main and $S1$ reflections appear at 1120 K. The present observations support this temperature dependence of the satellite reflections. Thus, the decrease in intensity of the $S1$ reflections can be explained by a reordering of the clusters. This reordering may correspond to the formation of decagonal superclusters (DSC), which are composed of five interpenetrating pentagonal superclusters (PSC), as reported in Part I. Consequently, this reordering takes place on the cost of the superstructure ordering formed by the PSCs.

To summarize, the structural disorder associated with the $S1$ reflections shows basically intercluster correlations only

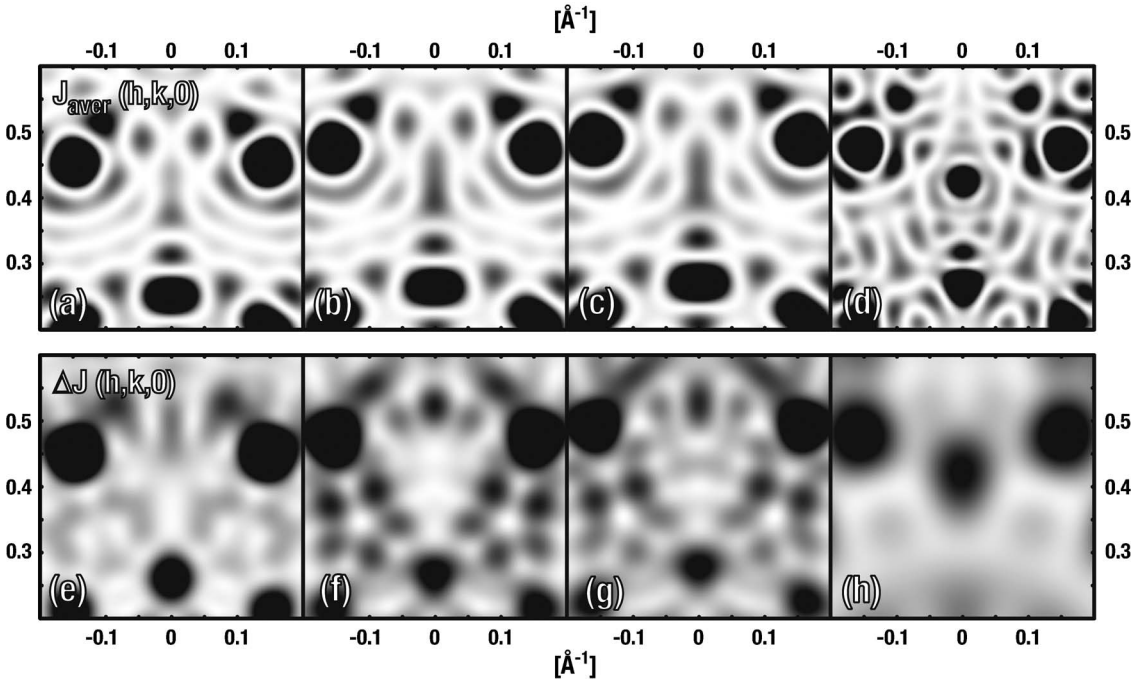

FIG. 13. Comparison of diffraction patterns of the cluster-models of Abe *et al.* (Ref. 24), Abe *et al.* (Ref. 23), Steinhardt *et al.* (Ref. 31), and Steurer *et al.* (Ref. 34). The cluster form factors of the average structures of fivefold orientationally disordered clusters are shown in (a)–(d), respectively. The corresponding diffuse diffraction intensities of fivefold orientationally disordered clusters in (e)–(h), respectively. The patterns in (a)–(d) and in (e)–(h) are on the same scale, respectively.

inside quasiperiodic layers. On the contrary, the *S*2 reflections are related to both intra- and intercluster correlations between adjacent and inside quasiperiodic layers.

E. Sensitivity of diffuse scattering intensities on cluster variations

Modeling disorder phenomena in quasicrystals can be used as a powerful tool for the selection of correct structure models. Small changes in cluster models also produce only small changes in the average structure of these clusters. If the atoms, which are affected by these small changes are involved in disorder, such small changes can have a great influence on the diffuse scattering intensities. Thus, a selection of correct structure models based only on the study of the average structures becomes very difficult and studying the diffuse scattering can be extremely helpful in this case. Figure 13 shows a comparison of diffraction patterns of average structures and diffuse scattering for different cluster-models. Zoomed sections of the cluster form factors of the average structures of fivefold orientationally disordered clusters are shown in Figs. 13(a)–13(d) for the structure models of Abe *et al.*,[24,23] Steinhardt *et al.*,[31] and Steurer *et al.*,[34] respectively. These patterns are governed by Bragg intensities only. Zoomed sections of the corresponding diffuse diffraction intensities of fivefold orientationally disordered clusters are shown in Figs. 13(e)–13(h), respectively. The atomic configurations of the first three clusters are very similar but the differences to the cluster of Steurer are more pronounced. Indeed, the diffraction patterns of the average structures reflect this coherency. Just by focusing on the diffraction patterns of the average structures, one cannot distinguish between the clusters of Abe *et al.*[23,24] and Steinhardt *et al.*[31] But taking into account the diffuse scattering, all four models can be distinguished.

VIII. CONCLUSIONS

The hydrodynamic theory of PDS and TDS was applied successfully to describe the short-range disordered structure of the *Edagawa phase*. Furthermore, modeling disorder on the scale of clusters showed that fivefold orientational disorder of the Abe cluster agrees best with experimental data. As a consequence, phasonic disorder and fivefold orientational disorder of the Abe cluster can be used equivalently to describe the short-range disordered structure of the *Edagawa phase*, i.e., orientational disorder of clusters is the 3D structural interpretation of phasonic disorder. Modeling of PDS associated with the *S*1 and *S*2 superstructure reflections indicates disorder of superclusters. The former shows basically intercluster correlations inside quasiperiodic layers, while the latter exhibits intra- and intercluster correlations, both between adjacent and inside quasiperiodic layers.

ACKNOWLEDGMENTS

The authors would like to thank the Swiss National Science Foundation for financial support by Project No. 20-67872.02. The authors also thank F. Frey for useful comments and the staff of the beamline D3 at the synchrotron source Hasylab for their assistance with the synchrotron measurements.

[1] M. de Boissieu, M. Boudard, B. Hennion, R. Bellissent, S. Kycia, A. Goldman, C. Janot, and M. Audier, Phys. Rev. Lett. **75**, 89 (1995).
[2] M. Boudard, M. de Boissieu, A. Letoublon, B. Hennion, R. Bellissent, and C. Janot, Europhys. Lett. **33**, 199 (1996).
[3] A. Létoublon, M. de Boissieu, M. Boudard, L. Mancini, J. Gastaldi, B. Hennion, R. Caudron, and R. Bellissent, Philos. Mag. Lett. **81**, 273 (2001).
[4] H. Abe, N. Tamura, D. Le Bolloc'h, S. C. Moss, Y. Matsuo, Y. Ishii, and J. M. Bai, Mater. Sci. Eng., A **294**, 299 (2000).
[5] H. Abe, Y. Matsuo, H. Saitoh, T. Kusawake, K. Ohshima, and H. Nakao, Jpn. J. Appl. Phys., Part 2 **39**, L1111 (2000).
[6] H. Abe, H. Saitoh, T. Kusawake, H. Nakao, Y. Matsuo, K. Ohshima, Y. Morikawa, and H. Matsumoto, J. Alloys Compd. **342**, 241 (2002).
[7] K. Edagawa, H. Sawa, and S. Takeuchi, Philos. Mag. Lett. **69**, 227 (1994).
[8] M. V. Jaric and D. R. Nelson, Phys. Rev. B **37**, 4458 (1988).
[9] J. Lei, R. Wang, C. Hu, and D. H. Ding, Phys. Rev. B **59**, 822 (1999).
[10] R. Wang, C. Hu, and J. Lei, Phys. Rev. B **61**, 5843 (2000).
[11] R. Wang, C. Hu, and J. Lei, Phys. Status Solidi B **225**, 21 (2001).
[12] Y. Ishii, Mater. Sci. Eng., A **294–296**, 377 (2000).
[13] W. Yang, C. Hu, D. H. Ding, and R. Wang, Phys. Rev. B **51**, 3906 (1995).
[14] C. Hu, R. Wang, W. Yang, and D. Ding, Acta Crystallogr., Sect. A: Found. Crystallogr. **A52**, 251 (1996).
[15] K. J. Strandburg, L. H. Tang, and M. V. Jaric, Phys. Rev. Lett. **63**, 314 (1989).
[16] L. H. Tang, Phys. Rev. Lett. **64**, 2390 (1990).
[17] L. J. Shaw, V. Elser, and C. L. Henley, Phys. Rev. B **43**, 3423 (1991).
[18] W.-J. Zhu and C. L. Henley, Europhys. Lett. **46**, 748 (1999).
[19] U. Koschella, F. Gähler, J. Roth, and H.-R. Trebin, J. Alloys Compd. **342**, 287 (2002).
[20] T. C. Lubensky, S. Ramaswamy, and J. Toner, Phys. Rev. B **32**, 7444 (1985).
[21] Y. Ishii, Phys. Rev. B **45**, 5228 (1992).
[22] W. Steurer, Z. Kristallogr. **219**, 391 (2004).
[23] E. Abe, K. Saitoh, H. Takakura, A. P. Tsai, P. J. Steinhardt, and H. C. Jeong, Phys. Rev. Lett. **84**, 4609 (2000).
[24] E. Abe, S. J. Pennycook, and A. P. Tsai, Nature (London) **421**, 347 (2003).
[25] K. Hiraga, F. J. Lincoln, and S. Wei, Mater. Trans., JIM **32**, 308 (1991).
[26] K. Hiraga, W. Sun, and A. Yamamoto, Mater. Trans., JIM **35**, 657 (1994).
[27] K. Hiraga, T. Ohsuna, W. Sun, and K. Sugiyama, Mater. Trans., JIM **42**, 2354 (2001).
[28] S. Ritsch, C. Beeli, and H. U. Nissen, Philos. Mag. Lett. **74**, 203 (1996).
[29] S. Ritsch, C. Beeli, and H. U. Nissen, Philos. Mag. Lett. **75**, 49 (1997).
[30] K. Saitoh, K. Tsuda, M. Tanaka, K. Kaneko, and A. P. Tsai, Jpn. J. Appl. Phys., Part 2 **36**, L1400 (1997).
[31] P. J. Steinhardt, H. C. Jeong, K. Saitoh, M. Tanaka, E. Abe, and A. P. Tsai, Nature (London) **396**, 55 (1998).
[32] P. J. Steinhardt, H. C. Jeong, K. Saitoh, M. Tanaka, E. Abe, and A. P. Tsai, Nature (London) **403**, 267 (2000).
[33] P. Gummelt, Geom. Dedic. **62**, 1 (1996).
[34] W. Steurer, T. Haibach, B. Zhang, S. Kek, and R. Lück, Acta Crystallogr., Sect. B: Struct. Sci. **49**, 661 (1993).
[35] Y. Yan, S. J. Pennycook, and A. P. Tsai, Phys. Rev. Lett. **81**, 5145 (1998).
[36] Y. Yan and S. J. Pennycook, Nature (London) **403**, 266 (2000).
[37] Y. Yan and S. J. Pennycook, Phys. Rev. B **61**, 14291 (2000).
[38] Y. Yan and S. J. Pennycook, Phys. Rev. Lett. **86**, 1542 (2001).
[39] K. Lemster, Ph.D. thesis ETH No. 14141, ETH Zurich, 2001.
[40] T. Haibach, A. Cervellino, W. Kek, and W. Steurer, HASYLAB Jahresber. **I**, 519 (1997).
[41] A. Cervellino, T. Haibach, and W. Steurer, Acta Crystallogr., Sect. B: Struct. Sci. **58**, 8 (2002).
[42] W. Steurer and T. Haibach, in *International Tables for Crystallography*, 2nd ed., edited by U. Shmueli (Kluwer Academic Publishers, Dordrecht, 2001), Vol. B, Chap. 4, pp. 486–532.
[43] E. N. Maslen, A. G. Fox and M. A. O'Keefe, in *International Tables for Crystallography*, edited by A. J. C. Wilson (Kluwer Academic Publishers, Dordrecht, 1992), Vol. C, Chap. 6.1, pp. 500–502.
[44] M. A. Chernikov, H. R. Ott, A. Bianchi, A. Migliori, and T. W. Darling, Phys. Rev. Lett. **80**, 321 (1998).
[45] J. M. Cowley, *Diffraction Physics*, 3rd rev. ed. (Elsevier Science B. V., Amsterdam, 1995).
[46] K. Niizeki, J. Phys. Soc. Jpn. **63**, 4035 (1994).
[47] K. Hiraga, T. Ohsuna, and S. Nishimura, Philos. Mag. Lett. **80**, 653 (2000).